

Heat and Mass Transfer Within an Evaporating Solution Droplet in a Plasma Jet

Yanguang Shan and Yuan Hu

(Submitted September 11, 2011; in revised form December 14, 2011)

Solution precursors have been injected into the plasma gases to produce finely structured ceramic coatings with nano- and sub-micrometric features. The trajectory history and heat and mass transfer within individual solution droplets play a very important role in determining the coating microstructure. A mathematical model is developed to analyse the thermal behavior of individual precursor droplets travelling in the high temperature plasma jet. This model involves the motion and evaporation of the precursor droplet in a DC plasma jet and the heat and mass transfer within the evaporating droplet. The influence of Stefan flow, as well as the variable thermo-physical properties of the solution and the plasma gas, is considered. The internal circulation due to the relative velocity between the droplet and the plasma jet, which may be approximated by the Hill vortex, is considered as well. The trajectory, temporal droplet surface temperature, and radius variation are predicted. The temporal temperature and concentration distributions within the evaporating droplet are presented for different injection parameters.

Keywords heat and mass transfer, mathematical model, plasma jet, solution droplets

1. Introduction

The conventional plasma spraying technology has been used to deposit ceramic and metallic coatings to provide wear, corrosion and heat resistance for components in many industrial applications in the last decades (Ref 1). This technique permits the injection of metallic and ceramic powders with a particle size between 10 and 100 μm into a high temperature and high velocity jet. These particles are melted and accelerated to the component surface to form the coating by stacking individual lamellae. The microstructure of coatings deposited by the conventional plasma spray is characterized with an anisotropic, layered structure, large lamellae boundaries with sizes from a few tens to a few hundreds micrometers, cracks, connected and open voids, and delaminations between the lamellae (Ref 2).

In the past decade, there has been a growing interest for manufacturing nanostructured materials due to their

enhanced properties. In the field of thermal spray coatings, effort has been devoted to develop plasma spray technologies which can deposit finely structured coatings with nano- and sub-micrometric features since the mid of 1990s (Ref 3, 4). Solution precursor plasma spray (SPPS) is one of the emerging techniques developed for attaining nano-structured ceramic coatings. In this technique, the solution precursor containing ceramic salts instead of ceramic powders is injected into a DC plasma jet either as a liquid stream or gas atomized droplets. The droplets in the size range of 5-100 μm , which is dependent on the injection modes (Ref 5), are injected into the plasma environment. While the droplets are rapidly heated up and accelerated, the solvent evaporates and results in the increase of the solute concentration. Evaporation of the precursor droplets results in the formation of solid or hollow shell particles which arrive on the substrate to generate the nano-microstructure of the coating (Ref 6, 7). This technology has been used to deposit thermal barrier coatings (Ref 8), gas sensors (Ref 9), and anodes and cathodes for fuel cells (Ref 10, 11). It also has potential for other applications such as depositing medical and photocatalytic coatings, etc. (Ref 2).

The coatings deposited by SPPS have fine splats and grains, cracks vertical to the substrate, and controlled micrometer and nanometer porosity. One of the most important factors that determine the coating microstructure is the heating and trajectory history of individual solution precursor droplets. The precursor droplets injected into the plasma jet undergo a sequence of physical and chemical processes. These include droplet breakup (and collisions for gas atomized droplets); solvent evaporation from the droplet surface; solute precipitation and pyrolysis; formation of the resultant particles of different morphologies; sintering, and perhaps melting of the product particles; and impact onto the substrate. In order to understand the physical and chemical processes that

This article is an invited paper selected from presentations at the 2011 International Thermal Spray Conference and has been expanded from the original presentation. It is simultaneously published in *Thermal Spray 2011: Proceedings of the International Thermal Spray Conference*, Hamburg, Germany, September 27-29, 2011, Basil R. Marple, Arvind Agarwal, Margaret M. Hyland, Yuk-Chiu Lau, Chang-Jiu Li, Rogerio S. Lima, and André McDonald, Ed., ASM International, Materials Park, OH, 2011.

Yanguang Shan and Yuan Hu, School of Energy and Power Engineering, University of Shanghai for Science and Technology, Shanghai, China. Contact e-mails: y.shan@utoronto.ca and shan@usst.edu.cn.

Nomenclature			
Variables			
A_r	averaging parameter	r	radius (m)
B_T, B_M	Spalding heat and mass transfer numbers	Re	Reynolds number
C_D	droplet drag coefficient	Sh	Sherwood number
C_P	specific heat (J/kg·°C)	T	temperature (K)
D	mass diffusivity of the vapor into the plasma (m ² /s)	t	time (s)
L	latent heat of vaporization (J/kg)	U	velocity in axial direction (m/s)
\dot{m}	vaporization rate (kg/s)	V	velocity in radial direction (m/s)
m_v	mass fractions of vapor	ρ	density (kg/m ³)
M	molecular weight (kg/kmol)	λ	thermal conductivity (w/m·k)
Nu	Nusselt number	μ	dynamic viscosity (kg/m·s)
P	pressure (Pa)	Subscripts	
Pe	Peclet number	g	gas mixture
Pr	Prandtl number	l	liquid
Q_g	heat transfer from the plasma gas to drop surface (J/s)	s	surface
Q_i	heat conduction from droplet surface into its interior (J/s)	v	vapor
		∞	far from the droplet

precursor droplets undergo in the plasma jet, studies have been carried out to investigate the transport phenomena and the heating and trajectory of solution droplets (Ref 6, 7, 12-15), influence of injection modes (Ref 5), and droplet breakup and collisions (Ref 14, 16-18). The infinite diffusivity model (Ref 5, 12, 17), the pure diffusion model (Ref 13) and the internal circulation model (Ref 6, 7) are used for the droplet evaporation in these works.

In this paper, a mathematical model is developed to analyze the thermal behavior of individual precursor droplets travelling in the high temperature plasma jet. For the plasma jet, 2D distributions of the temperature and velocity fields are provided. The model is employed to simulate the trajectory history and heat and mass transfer within individual $Ce(NO_3)_3 \cdot 6H_2O$ (dissolved in water) solution droplets in an argon plasma jet. The influence of the Stefan flow, as well as the variable thermo-physical properties of the solution and the plasma gas, is considered. The internal circulation due to the relative velocity between the droplet and the plasma jet, which may be approximated by the Hill vortex, is considered as well. The trajectory of the droplet and the temporal droplet surface temperature and radius variation are predicted. The temporal temperature and concentration distributions within the evaporating droplet are presented for different injection parameters.

2. Mathematical Models

The droplet is transversely injected into the plasma jet as shown in Fig. 1. In the previous models, one-dimensional flow field is considered (Ref 19), or the radial velocity component of the jet is neglected in the radial momentum equation of the droplet (Ref 6). In this work, the plasma temperature and velocity fields are predicted

from the computational model developed in Ref 12, and 2-D distributions of the plasma temperature and velocity fields are adopted as known conditions. The simulation is run for an argon plasma jet issuing into air surroundings. The argon flow rate is 35.4 slpm and the plasma power input is 13.86 kW ($V=15.4$ V, $I=900$ A). The plasma temperature and velocity fields are shown in Fig. 2 and 3, respectively. The predicted fields are used to perform the calculations for the injection of individual solution droplets into the plasma jet. In the calculations, one-way coupling between the droplet and the jet is assumed since the influence of the evaporation of an individual droplet on the plasma fields is negligible.

When the precursor droplets are injected into the plasma jet, they are accelerated downstream by the plasma flow toward the substrate. During this process, the droplets are heated up and the solvent vaporizes resulting in a decrease of the droplet size and an increase of concentration of the solute in the vaporizing droplets. The precipitation takes place at the zone where the concentration

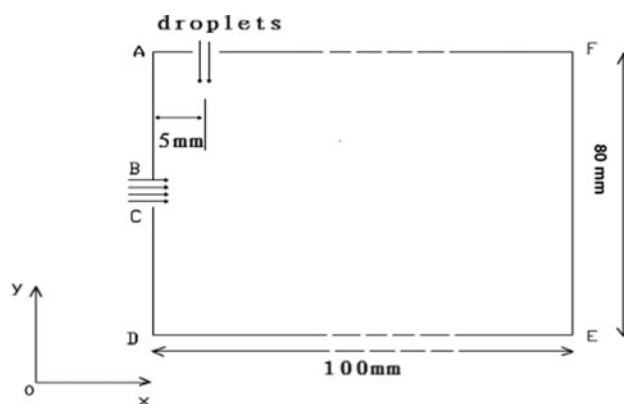


Fig. 1 The computational domain

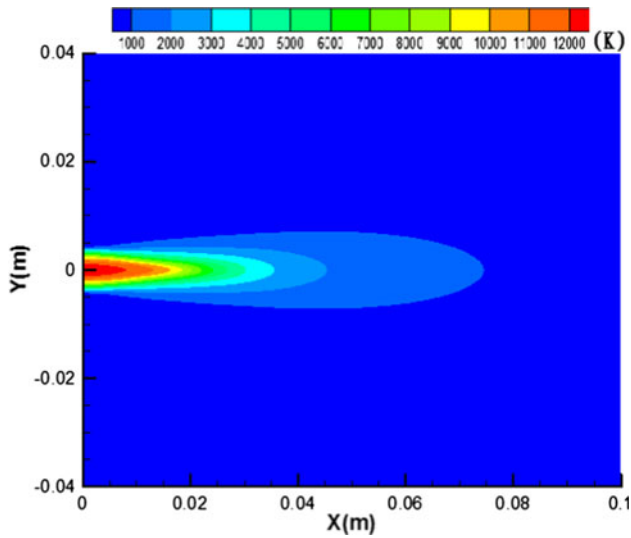


Fig. 2 The temperature field of the plasma jet

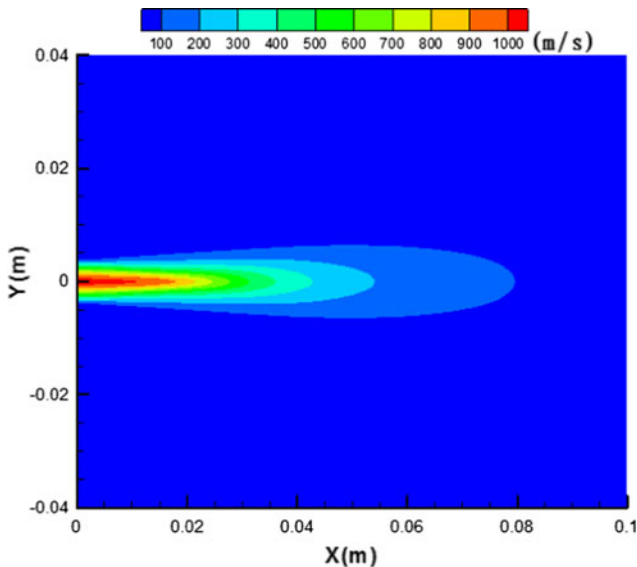


Fig. 3 The velocity field of the plasma jet

of the droplet reaches the critical saturation solute concentration. In this work, we focus on the trajectory history of the droplet and heat and mass transfer within the vaporizing droplet. The calculation stops as the droplet precipitation occurs.

For simplicity, the following assumptions are employed in this model: (1) the droplet is assumed to be spherical; (2) the influence of vaporizing droplets on the plasma is negligible; (3) only a single droplet is considered, the effect of neighboring droplets is neglected; (4) the gas/vapor phase surrounding the droplet is in quasi-steady state; (5) only aerodynamic drag force is considered for the droplet motion, the gravitational and thermophoretic forces are assumed to be negligible; (6) the gas-liquid interface is

always in thermodynamic equilibrium; and (7) the radiation of the droplet and the rarefaction effect are neglected.

2.1 Droplet Motion

The droplet motion and radius variation are governed by the following equations:

$$\frac{\partial U}{\partial t} = \frac{3C_D}{8r_s} \frac{\rho_\infty}{\rho_L} |U_\infty - U|(U_\infty - U) \quad (\text{Eq 1})$$

$$\frac{\partial V}{\partial t} = \frac{3C_D}{8r_s} \frac{\rho_\infty}{\rho_L} |V_\infty - V|(V_\infty - V) \quad (\text{Eq 2})$$

$$\frac{\partial r_s}{\partial t} = -\frac{\dot{m}}{4\pi\rho_L r_s^2} \quad (\text{Eq 3})$$

where U , V , r_s are the axial and radial velocity and the instantaneous radius of the droplet, respectively, U_∞ , V_∞ , and ρ_∞ are the axial and radial velocity and density of the plasma jet, respectively. \dot{m} is the vaporization rate at the droplet surface, which can be obtained from the heat and mass transfer model between the droplet and the jet. C_D is the droplet drag coefficient which is calculated as follows (Ref 6).

$$C_D = \frac{24}{Re(1 + B_M)} \quad (\text{Eq 4})$$

The Reynolds number is defined as:

$$Re = 2\rho_\infty |U_\infty - U| r_s / \mu_g \quad (\text{Eq 5})$$

μ_g is the average viscosity of the plasma gas and vapor near the droplet surface, which is evaluated at the following reference temperature and droplet concentration.

$$T = T_s + A_r(T_\infty - T_s) \quad (\text{Eq 6})$$

$$m_s = m_{vs} + A_r(m_{v\infty} - m_{vs}) \quad (\text{Eq 7})$$

where $A_r = 1/3$ is recommended (1/3 rule).

2.2 Heat and Mass Transfer Between the Droplet and the Plasma Gas

To obtain the trajectory and the instantaneous radius variation, the expressions of the droplet vaporization rate \dot{m} and the droplet surface temperature should be provided. The analysis of heat and mass transfer between the droplet and the plasma gas, which is based on the well known 'film theory' and quasi-steady heat and mass transfer assumptions, yields the expressions of the instantaneous vaporization rate \dot{m} and the amount of heat transferred into the droplet (Ref 20).

$$\dot{m} = 2\pi\rho_g D r_s \text{Sh}[\ln(1 + B_M)] \quad (\text{Eq 8})$$

$$\dot{m} = 2\pi \frac{\lambda_g}{C_{pv}} r_s \text{Nu}[\ln(1 + B_T)] \quad (\text{Eq 9})$$

ρ_g , C_{pv} , λ_g are the average density, the average specific heat, and the thermal conductivity of the mixed gas in the

film, respectively. They are evaluated using the 1/3 rule. D is the mass diffusivity of vapor phase into the plasma gas; B_M , B_T are the Spalding mass and heat transfer numbers which are calculated as follows.

$$B_M = \frac{m_{vs} - m_{v\infty}}{1 - m_{vs}} \quad (\text{Eq 10})$$

$$B_T = \frac{C_{pv}(T_\infty - T_s)}{L + Q_g/\dot{m}} \quad (\text{Eq 11})$$

where m_{vs} , $m_{v\infty}$ are the mass fractions of vapor at the droplet surface and in the plasma at far field, respectively. For the single droplet, $m_{v\infty} = 0$, $m_{vs} = (P_{vs}M_v/P_\infty\bar{M})$; P_{vs} is the saturated vapor pressure at the droplet's temperature which is evaluated by Clausius-Clapeyron equation; P_∞ is the plasma environment pressure; M_v is the molecular weight of the vapor; \bar{M} is the average molecular weight of all species.

Nu and Sh are the Nusselt and Sherwood numbers, respectively. In consideration of the Stefan flow, which influences the thicknesses of the gas film, the universal correction factor $F(B)$ is introduced:

$$F(B) = (1 + B)^{0.7} \frac{\ln(1 + B)}{B} \quad (\text{Eq 12})$$

Then the corrected Sh and Nu are given by (Ref 21):

$$Sh = \left(2 + \frac{0.552Re^{1/2}Sc^{1/3}}{F(B_M)}\right) \frac{\ln(1 + B_M)}{B_M} \quad (\text{Eq 13})$$

$$Nu = \left(2 + \frac{0.552Re^{1/2}Pr^{1/3}}{F(B_T)}\right) \frac{\ln(1 + B_T)}{B_T} \quad (\text{Eq 14})$$

At the droplet's surface, the energy balance is expressed as:

$$Q_g = \dot{m}L + Q_i \quad (\text{Eq 15})$$

Q_g is the heat transferred from the plasma gas to the drop surface and it is given by:

$$Q_g = 2\pi\lambda_\infty(T_\infty - T_s)Nu \quad (\text{Eq 16})$$

Q_i is the heat penetrating into the droplet interior which is calculated as:

$$Q_i = \frac{4}{3}\pi r_s^3 C_p \frac{dT_s}{dt} \quad (\text{Eq 17})$$

These equations along with the Clapeyron equation and Raoult's law are solved to determine the droplet vaporization rate and the droplet surface temperature.

2.3 Heat and Mass Transfer Within the Droplet

Due to the relative velocity between the droplet and the plasma gas, the internal circulation within the droplet is induced by the surface friction. It has been suggested by Sirignano that the instantaneous velocity field inside the moving droplet may be approximated by the well-known

Hill vortex in the spherical coordinate system (r, θ) (Ref 22):

$$V_r = U_s(1 - r^2/r_s^2) \cos \theta \quad (\text{Eq 18})$$

$$V_\theta = U_s(1 - 2r^2/r_s^2) \sin \theta \quad (\text{Eq 19})$$

U_s is the maximum surface velocity which is expressed as:

$$U_s = \frac{1}{32} \Delta U_\infty \left(\frac{\mu_g}{\mu_L}\right) Re_\infty C_F \quad (\text{Eq 20})$$

where C_F is the friction drag coefficient in the following correlation considering the effect of the Stefan flow:

$$C_F = \frac{12.69}{Re^{2/3}(1 + B_M)} \quad (\text{Eq 21})$$

The governing equations of the heat and mass transfer within the droplet may be expressed as the universal conservation equation.

$$\frac{\partial}{\partial t}(\rho\Phi) + \text{div}(\rho u\Phi) = \text{div}(\Gamma \text{grad}\Phi) + S \quad (\text{Eq 22})$$

The initial and boundary conditions are given as:

$$\tau = 0, T = T_0, m_1 = m_{10} \quad (\text{Eq 23})$$

$$r = r_s, \frac{\partial T}{\partial r} = \frac{Q_i}{4\pi r_s^2 \lambda_L}, \frac{\partial m_1}{\partial r} = \frac{\dot{m}}{4\pi r_s^2 \rho_L D_L} \quad (\text{Eq 24})$$

$$\theta = 0, \pi, \frac{\partial T}{\partial \theta} = 0, \frac{\partial m_1}{\partial \theta} = 0 \quad (\text{Eq 25})$$

The trajectory, velocity and instantaneous radius of the droplets are obtained from the droplet motion model. The heat and mass transfer model between the plasma gas and the droplet provides the vaporization rate and the heat transferred into the droplet. They are used as the boundary conditions in solving the model of heat and mass transfer within the moving droplet. Once the mass and energy equations are solved, the temperature and concentration distributions within the droplet can be predicted.

3. Results and Discussion

The model is used to simulate the trajectory history and heat and mass transfer within individual $\text{Ce}(\text{NO}_3)_3 \cdot 6\text{H}_2\text{O}$ (dissolved in water) solution droplets in an argon plasma jet. The properties of the plasma gas are obtained from Ref 23, and the properties of $\text{Ce}(\text{NO}_3)_3 \cdot 6\text{H}_2\text{O}$ solution are obtained from Ref 24. Calculations are performed for 20, 30, 40, and 60 μm droplet sizes, and 15, 20 and 25 m/s droplet injection velocities to investigate their effects on the trajectory and vaporization of the droplet. The temporal temperature and concentration distributions within the evaporating droplet are predicted for these conditions. It is assumed that the precipitation takes place at the

droplet surface when the solute concentration at the droplet surface reaches a critical saturation solute concentration (set as 1.0 in this work). The simulation stops at this point and the trajectory and heating (or vaporization) of the droplet after the precipitation are not presented.

3.1 Trajectory and Vaporization of the Droplet with Different Injection Velocities

The simulations are performed for $30\ \mu\text{m}$ $\text{Ce}(\text{N}-\text{O}_3)_3 \cdot 6\text{H}_2\text{O}$ solution (solvent is water) droplets with injection velocities of 15, 20 and 25 m/s, respectively. The initial droplet temperature is 300 K and the solute concentration is 0.3. The injector is located 5 mm downstream of the plasma gun exit, and 10 mm away from the jet centerline (Fig. 1). The trajectory and variation of droplet size are presented in Fig. 4. The plasma temperature that the droplets experience and the temporal droplet surface temperature are presented in Fig. 5. The droplets penetrate into the hot plasma gas and are heated up and accelerated to the substrate (Fig. 4a). During the early stage of the trajectory, the droplet travels in the outer zone of the jet and its surface temperature decreases a little bit below the temperature of the environment due to the cooling effect of the vaporization (Fig. 5a). The

vaporization rate is low and the droplet size almost remains unchanged (Fig. 4b). After this stage (about 0.25, 0.35, and 0.45 ms for the droplet with injection velocities of 15, 20 and 25 m/s, respectively), the droplet surface temperature increases rapidly along its trajectory (Fig. 5a), and the solvent (water) vaporizing from the droplet surface results in the rapid decrease of the droplet size (Fig. 4b). It is shown that the droplet with the higher injection velocity penetrates deeper than the droplet with the lower velocity due to its higher momentum (Fig. 4a). As a result, the droplet with higher injection velocity experiences higher plasma temperature (Fig. 5b), and the variation of the surface temperature and the decrease of droplet size are faster.

3.2 Temperature and Solute Concentration Distributions Within the Droplet with Different Injection Velocities

The temperature and solute concentration distributions within the moving droplet with different injection velocities are shown in Fig. 6. At the very early stage of the droplet trajectory, the droplet travels in the outer zone of the jet where the plasma temperature and velocity are low. Consequently, the relative velocity between the droplet

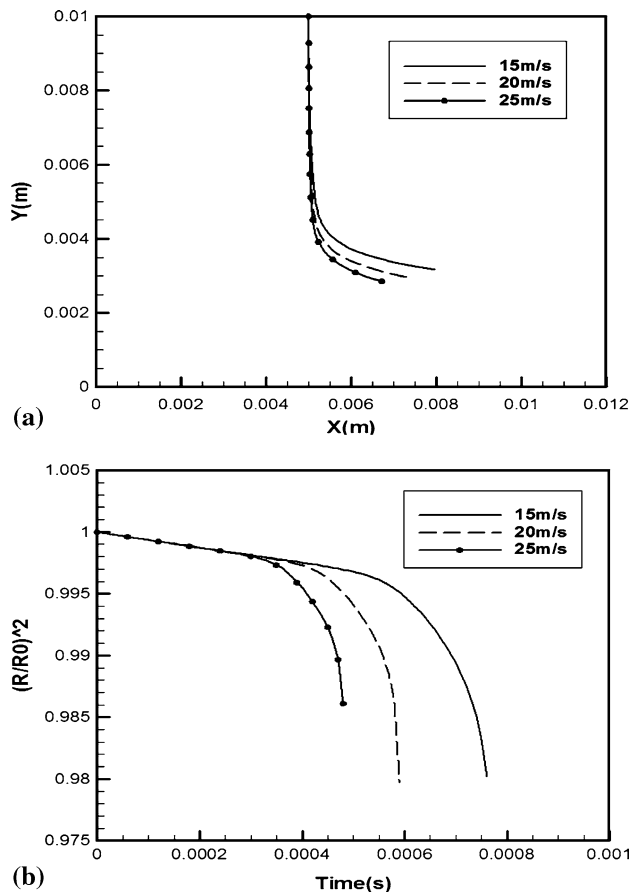


Fig. 4 The trajectory (a) and variation of droplet size (b) for different injection velocities

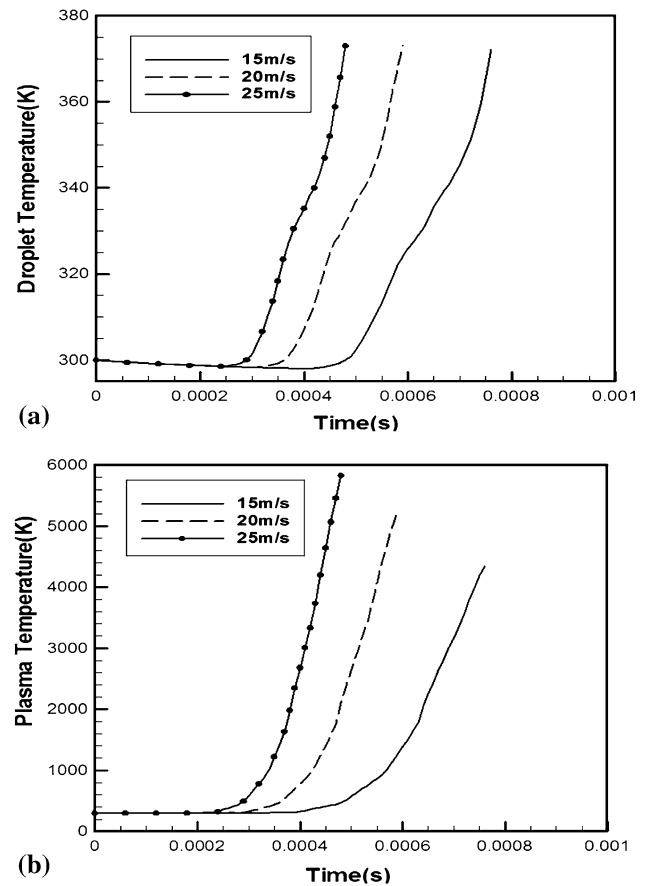


Fig. 5 The temporal droplet surface temperature (a) and the plasma temperature experienced by the droplets (b) for different injection velocities

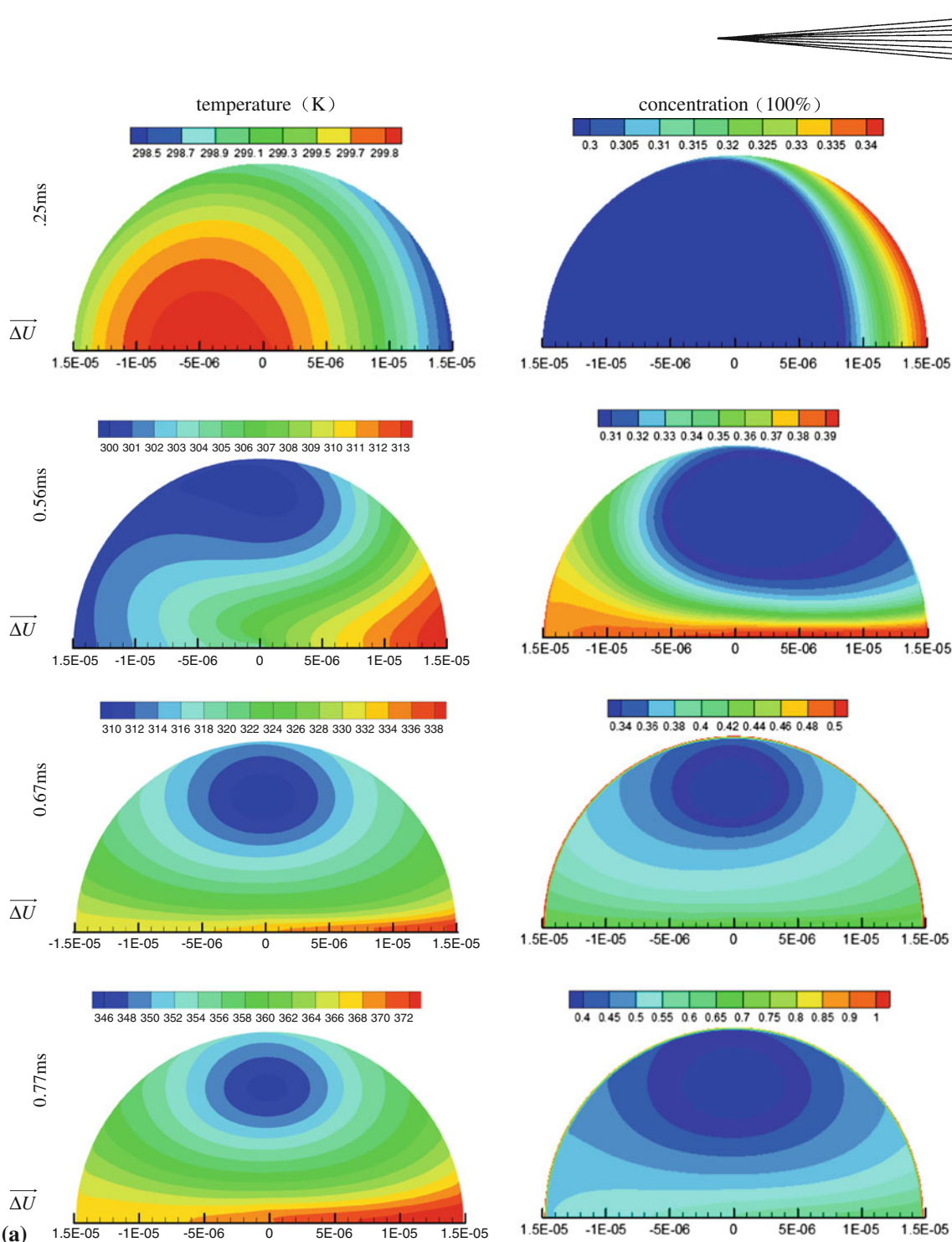


Fig. 6 Temperature and solute concentration distributions within the 30 μm droplet with different injection velocities: (a) 15 m/s; (b) 20 m/s; and (c) 25 m/s

and the plasma gas is low. The internal convection is weak at this stage, and the heat is transferred into the droplet interior from the surface primarily by the thermal conduction. The temperature and solute concentration distributions show pure diffusion characteristics (0.25 ms in Fig. 6a-c). Along the trajectory, the droplet penetrates deeper into the plasma jet, the relative velocity between the droplet surface and the plasma gas increases, the convection effect increases and the distributions become

distorted and show both diffusion and convection characteristics (0.56 ms in Fig. 6a, 0.43 ms in Fig. 6b, and 0.35 ms in Fig. 6c). The transition from conduction to convection depends on the droplet Pe_L number. At the later stage, the Peclet number becomes high with the increase of the relative velocity, and the temperature and solute concentration distributions within the droplet coincide with the streamlines (after 0.56 ms in Fig. 6a, 0.43 ms in Fig. 6b, and 0.35 ms in Fig. 6c). It should be

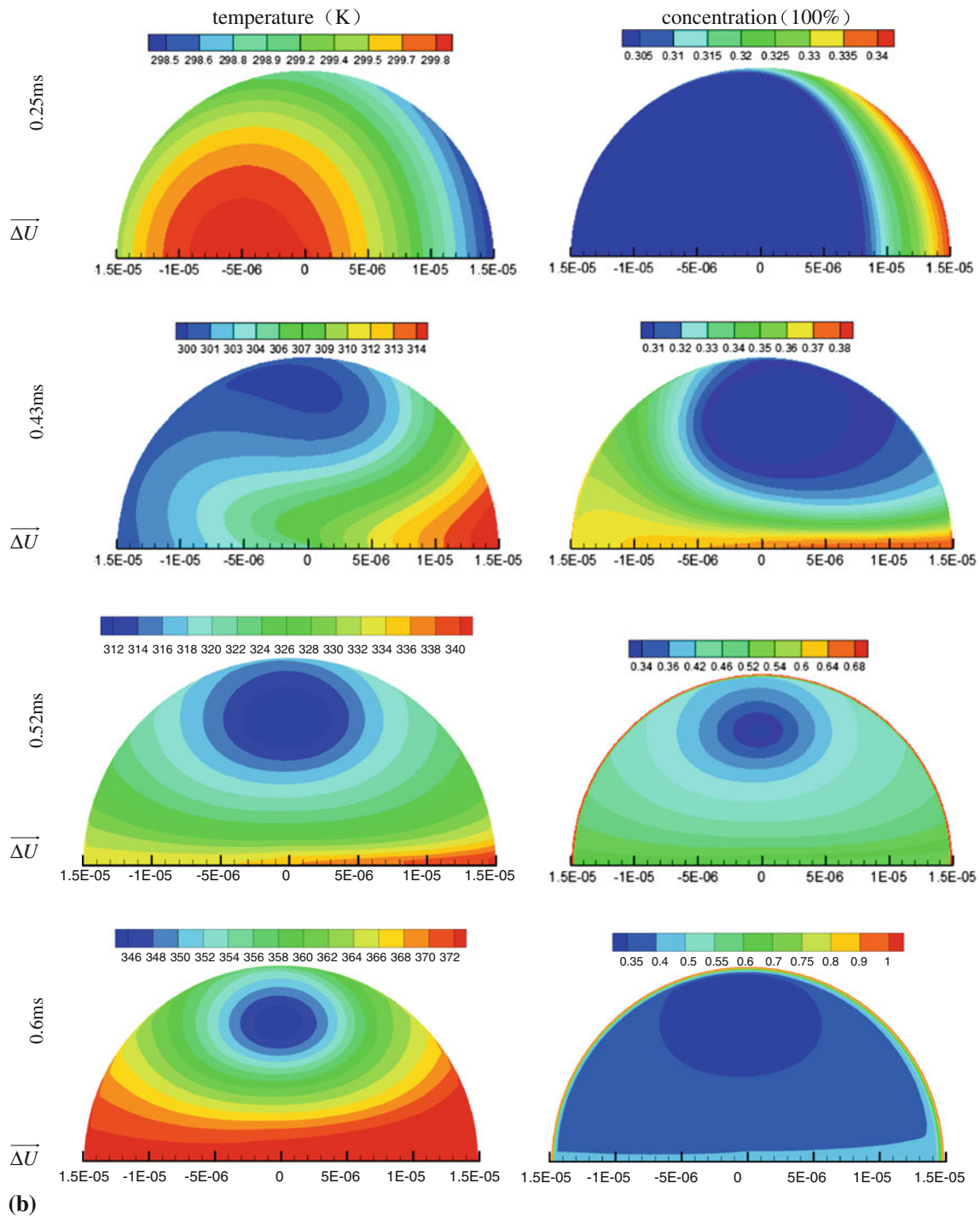


Fig. 6 Continued

noted that for a pure liquid droplet experiencing the last stage of its trajectory, the internal transport mechanism becomes diffusion-dominated since the relative velocity between the droplet and the plasma gas decreases to zero. For the solution droplet, the evaporation of the solvent results in the increase of the solute concentration at the droplet surface (Fig. 6). When it reaches the critical saturation concentration, volume or shell precipitation occurs

depending on the nature of the substance and the solute distributions within the droplet (Ref 25). The internal heat transfer mechanism for the solid particle is pure conduction, the heat and mass transfer mechanism for the droplet contained in the shell is complicated (Ref 24), and is not included in this work.

It is also shown in Fig. 6 that the temperature distributions within the droplets for different injection

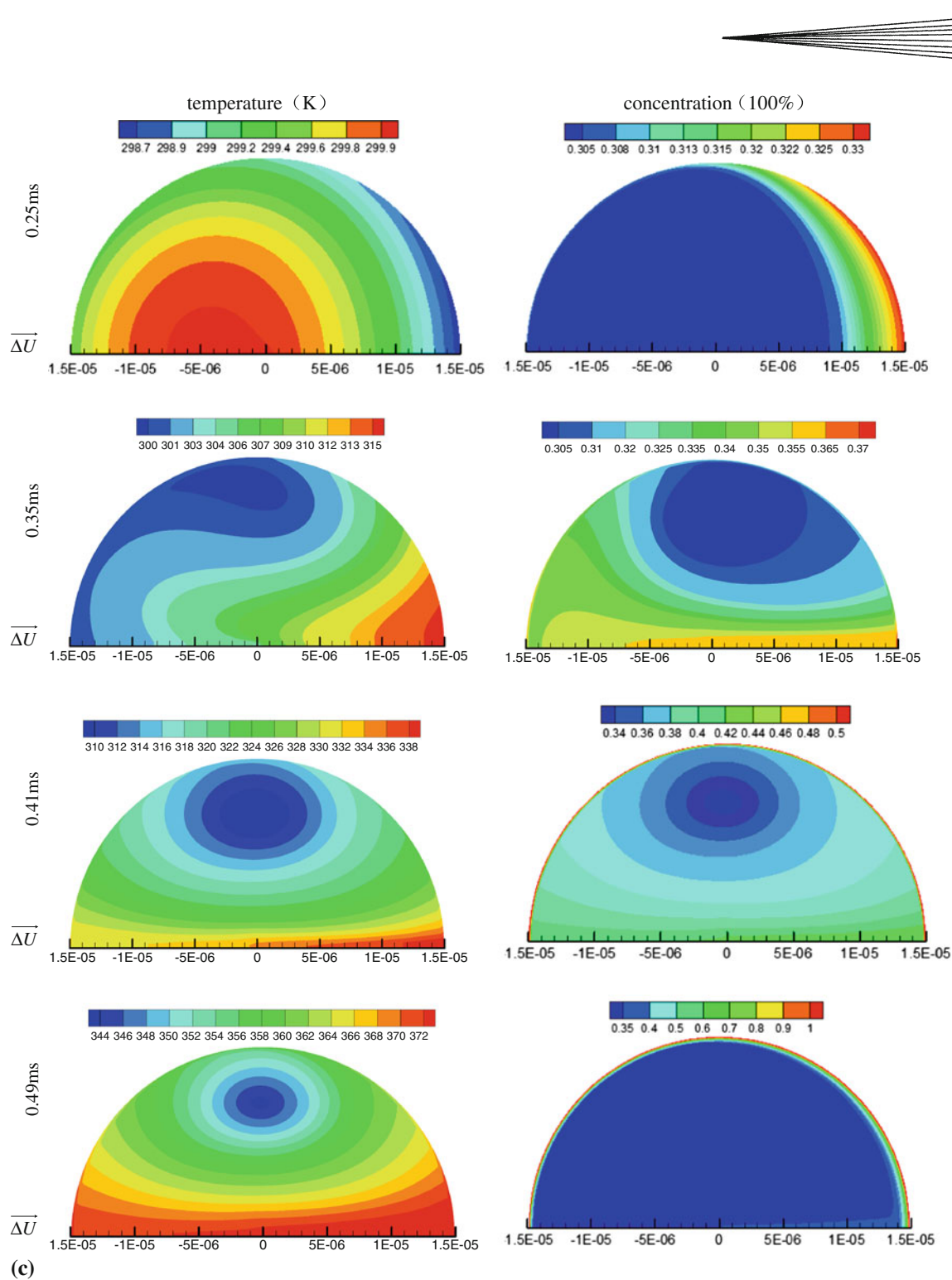


Fig. 6 Continued

velocities exhibit similar characteristics, while the solute concentration distribution in the droplet with the lower injection velocity is more uniform than that with the higher injection velocity. The solute concentrates at the droplet surface due to the higher degree of internal convection for the droplet with the higher injection velocity. As a result, the possibility of shell precipitation is high for such droplets, and the possibility of volume

precipitation is high for droplets with the lower injection velocity.

3.3 Trajectory and Vaporization of the Droplet with Different Initial Sizes

The simulations are performed for 20, 40, and 60 μm $\text{Ce}(\text{NO}_3)_3 \cdot 6\text{H}_2\text{O}$ solution droplets with the injection

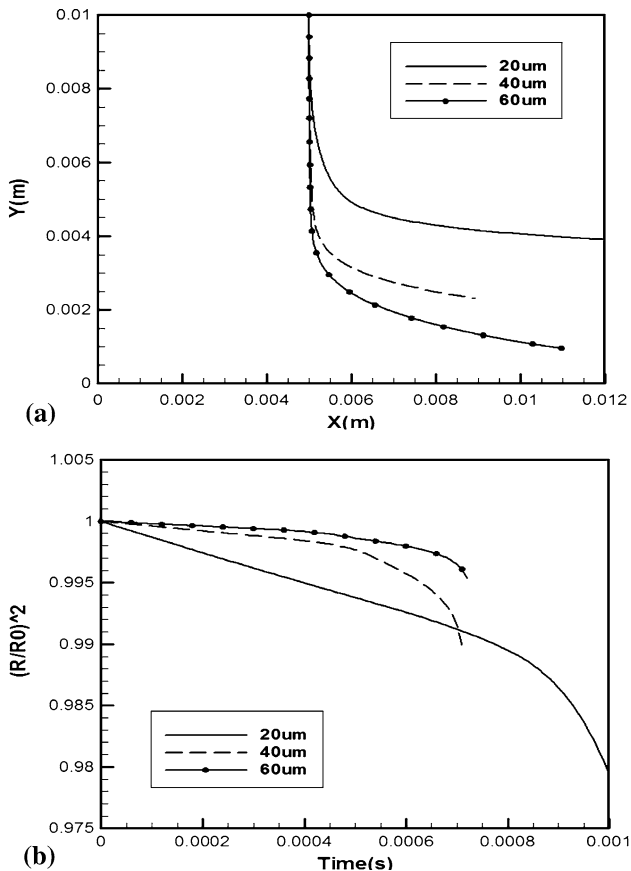


Fig. 7 The trajectory (a) and variation of the droplet size (b) for different initial droplet diameters

velocity of 15 m/s. The other conditions are the same as in Section 3.1. The trajectory and variation of droplet size are presented in Fig. 7. During the early stage of the trajectory and heating, the heat is transferred into the droplet interior from the surface primarily by the thermal conduction as discussed in Section 3.2. Since the droplets with different sizes experience almost the same plasma temperature at this stage, the vaporization rate for the larger droplet is lower than that of smaller droplets due to its large mass and low specific surface area (Fig. 7b). After this stage, the droplet surface temperature increases rapidly along its trajectory. The temperatures of the droplets uniformly increase and the internal circulation becomes stronger in the droplets. The heat is effectively transferred into the droplet interior by convection. The vaporization rate of a 40 μm droplet becomes the fastest, while the vaporization rate of a 60 μm droplet is still low since more heat is required to heat up the droplet. Another reason is that the solvent concentration at the larger droplet surface is lower than that of smaller droplets at this stage, which will be illustrated in Section 3.4. This also contributes to the low vaporization rate of the 60 μm droplet. The vaporization rate of a 20 μm droplet is lower than that of a 40 μm droplet because the internal circulation inside the

20 μm droplet is weaker. It is shown from Fig. 7a that the larger droplet penetrates deeper than the smaller droplet due to its higher momentum. As a result, the larger droplet experiences higher plasma temperatures. (For very large droplets, they pass through the hot core of the jet and the temperatures they experience decrease.) The fact that the vaporization rate of the 60 μm droplet is not the fastest indicates that the vaporization of the droplet is determined not only by the environment temperature and external heat and mass transfer mechanism, but also by the internal heat and mass transfer mechanism.

3.4 Temperature and Solute Concentration Distributions Within the Droplet with Different Initial Sizes

The temperature and solute concentration distributions within the droplets with the initial sizes of 20, 40 and 60 μm and 15 m/s injection velocity are shown in Fig. 8. As discussed above, at the very early stage of the droplet trajectory, the temperature and solute concentration distributions show pure diffusion characteristics. Along the trajectory, the convection effect increases and the distributions become distorted and show both diffusion and convection characteristics. At the later stage, the temperature and solute concentration distributions within the droplet coincide with the streamlines due to the high droplet Peclet number. It is shown in Fig. 8 that the temperature distributions within the droplets for different initial sizes exhibit similar evolution characteristics, while the solute concentration distribution in the smaller droplet (20 μm) is more uniform than that of the larger droplet (40, 60 μm). It is also shown that the solute concentration at the 60 μm droplet surface is higher than that of the 40 μm droplet due to the higher degree of internal convection. As mentioned above, this may decrease the vaporization rate of the 60 μm droplet. Since the solute concentration distribution in the smaller droplet (20 μm) is more uniform, and the interior of the droplet could reach the critical saturation concentration when the precipitation occurs at its surface, the possibility of volume precipitation is high for the smaller droplet. The possibility of shell precipitation is high for the large droplet due to its non-uniform distribution of the solute concentration.

4. Conclusions

A mathematical model is developed to analyze the thermal behavior of individual precursor droplets traveling in the high temperature plasma jet. The model is employed to simulate the trajectory history and heat and mass transfer within individual $\text{Ce}(\text{NO}_3)_3 \cdot 6\text{H}_2\text{O}$ (dissolved in water) solution droplets in an argon plasma jet. The trajectory of the droplet and the temperature and solute concentration distributions within the droplet are predicted for different injection velocities and initial droplet sizes. The results indicate that the droplets with high

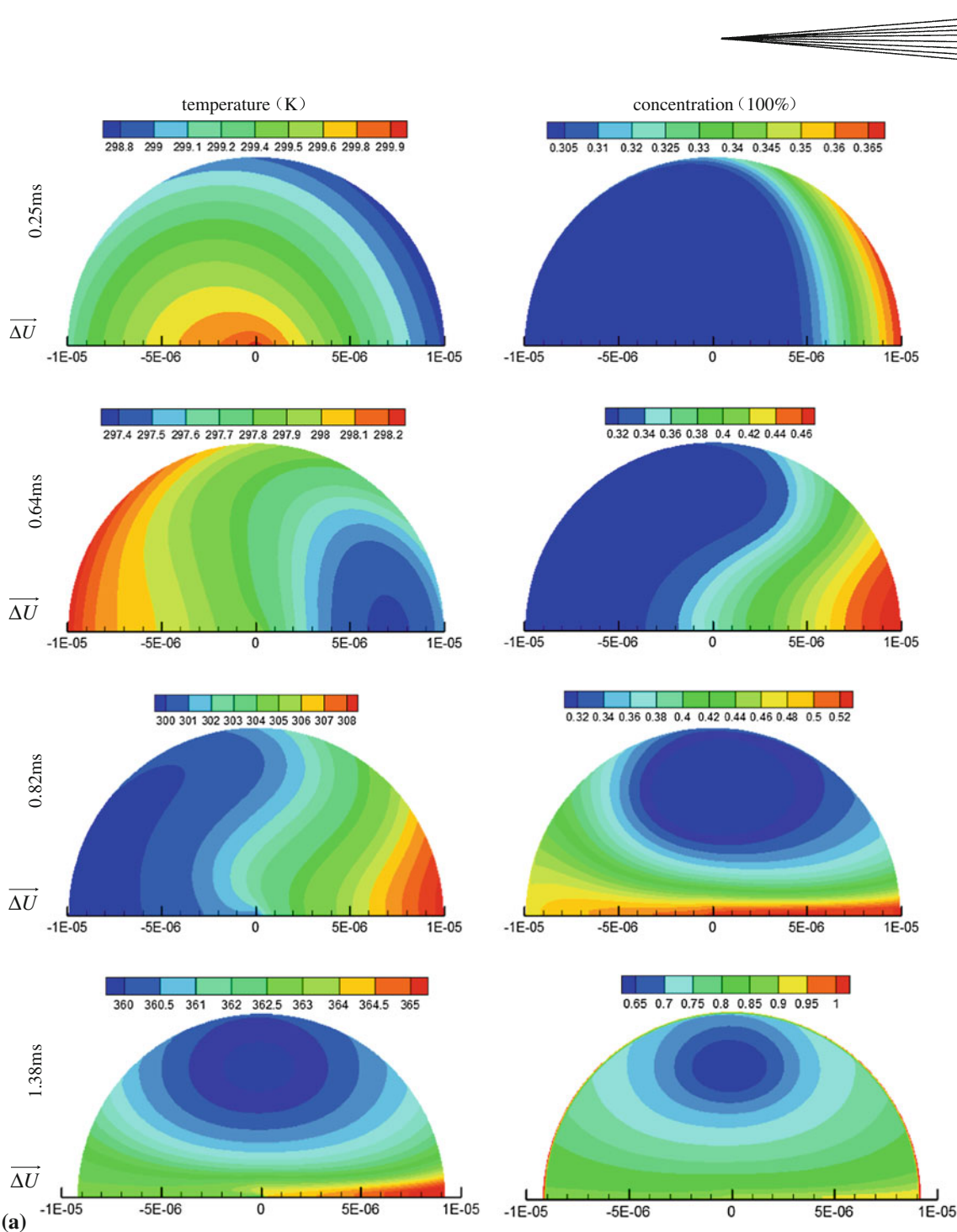


Fig. 8 Temperature and solute concentration distributions within the droplets of different initial diameters (the injection velocity is 15 m/s): (a) 20 μm ; (b) 40 μm ; and (c) 60 μm

momentum (high injection velocity or large mass) penetrate deeper into the plasma jet and experience high plasma temperatures and velocities. For the droplets with higher injection velocities, the variation of the surface temperature and the vaporization of the droplet are faster. The larger droplets exhibit different vaporization behaviour. It is possible that the larger droplets experiencing

high plasma temperatures may have a lower vaporization rate. The results also indicate that the temperature and solute concentration distributions within the droplets highly depend on the transport mechanism inside the droplet (diffusion-dominated or convection dominated). The solute concentration distributions inside smaller droplets or droplets with the lower injection velocities are

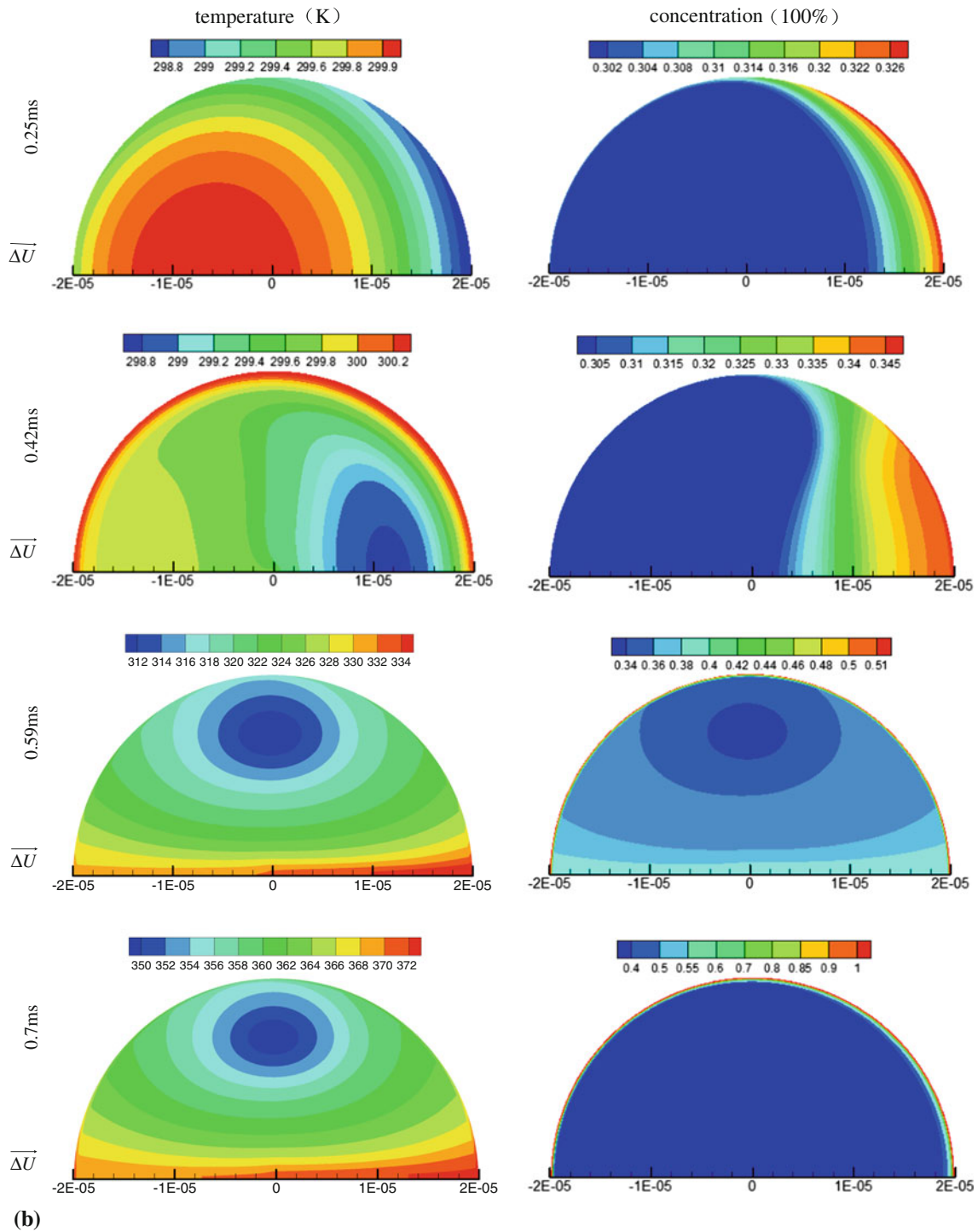


Fig. 8 Continued

more uniform than that of larger droplets or droplets with the higher injection velocities. As a result, shell precipitation probably occurs for the larger droplets or droplets

with higher injection velocities, while volume precipitation occurs for the smaller droplets or droplets with the lower injection velocities.

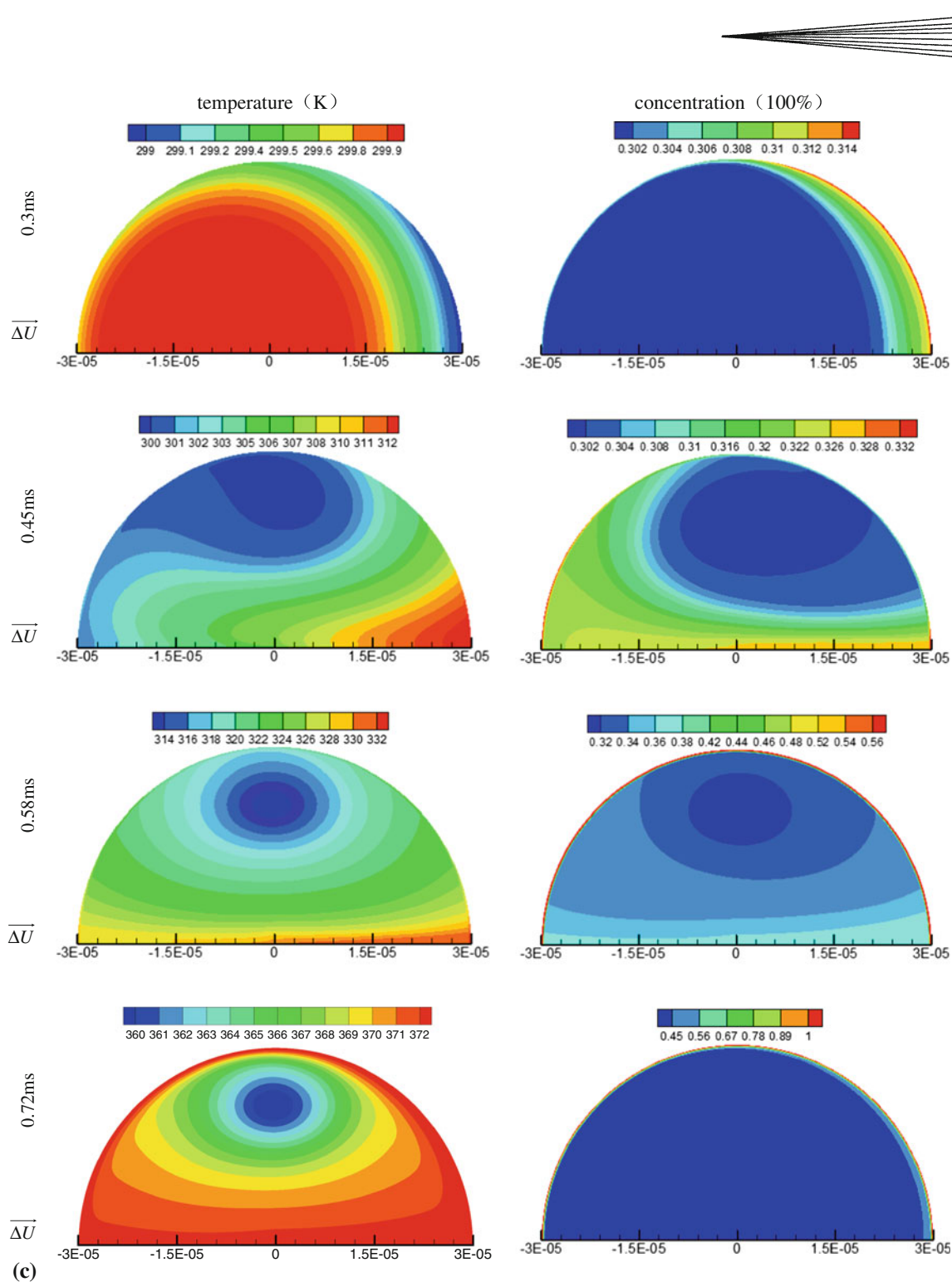


Fig. 8 Continued

Acknowledgments

The financial support of the National Natural Science Foundation of China (Project 50706027), the Scientific Research Foundation for the Returned Overseas Chinese Scholars, and Shanghai Leading Academic Discipline Project (Project J50501) are gratefully acknowledged.

References

1. P. Fauchais, A. Vardelle, and B. Dussoubs, Quo Vadis Thermal Spraying?, *J. Therm. Spray Technol.*, 2001, **10**, p 44-66
2. P. Fauchais, G. Montavon, R. Lima, and B. Marple, Engineering a New Class of Thermal Spray Nano-Based Microstructures from Agglomerated Nanostructured Particles, Suspensions and Solutions: An Invited Review, *J. Phys. D Appl. Phys.*, 2011, **44**, p 1-53

3. J. Karthikeyan, C. Berndt, S. Reddy, J. Wang, A. King, and H. Herman, Nanomaterial Deposits Formed by DC Plasma Spraying of Liquid Feedstocks, *J. Am. Ceram. Soc.*, 1998, **81**, p 121-128
4. N. Padture, K. Schlichting, T. Bhatia, A. Ozturk, B. Cetegen, E. Jordan, and M. Gell, Towards Durable Thermal Barrier Coatings with Novel Microstructures Deposited by Solution-Precursor Plasma Spray, *Acta Mater.*, 2001, **49**, p 2251-2257
5. Y. Shan, T. Coyle, and J. Mostaghimi, Modeling the Influence of Injection Modes on the Evolution of Solution Sprays in a Plasma Jet, *J. Therm. Spray Technol.*, 2010, **19**, p 248-254
6. A. Ozturk and B. Cetegen, Modeling of Plasma Assisted Formation of Precipitates in Zirconium Containing Liquid Precursor Droplets, *Mater. Sci. Eng. A*, 2004, **384**, p 331-351
7. A. Ozturk and B. Cetegen, Modeling of Axially and Transversely Injected Precursor Droplets into a Plasma Environment, *Int. J. Heat Mass Transf.*, 2005, **48**, p 4367-4383
8. L. Xie, X. Ma, E. Jordan, N. Padture, D. Xiao, and M. Gell, Deposition of Thermal Barrier Coatings Using the Solution Precursor Plasma Spray Process, *J. Mater. Sci.*, 2004, **39**, p 1639-1646
9. T. Chien and T. Coyle, Rapid and Continuous Deposition of Porous Nanocrystalline SnO₂ Coating with Interpenetrating Pores for Gas Sensor Applications, *J. Therm. Spray Technol.*, 2007, **16**, p 886-892
10. T. Coyle and Y. Wang, Solution Precursor Plasma Spray of Nickel-Yttria Stabilized Zirconia Anodes for Solid Oxide Fuel Cell Application, *J. Therm. Spray Technol.*, 2007, **16**, p 898-904
11. T. Coyle and Y. Wang, Solution Precursor Plasma Spray of Porous La_{1-x}Sr_xMnO₃ Perovskite Coatings for SOFC Cathode Application, *J. Fuel Cell Sci. Technol.*, 2011, **8**, p 021005
12. Y. Shan, T. Coyle, and J. Mostaghimi, 3D Modeling of Transport Phenomena and the Injection of the Solution Droplets in the Solution Precursor Plasma Spraying, *J. Therm. Spray Technol.*, 2007, **16**, p 736-743
13. S. Basu and B. Cetegen, Modeling of Thermo-Physical Processes in Liquid Ceramic Precursor Droplets Injected into a Plasma Jet, *Int. J. Heat Mass Transf.*, 2007, **50**, p 3278-3290
14. S. Basu, E. Jordan, and B. Cetegen, Fluid Mechanics and Heat Transfer of Liquid Precursor Droplets Injected into High-Temperature Plasmas, *J. Therm. Spray Technol.*, 2008, **17**, p 60-72
15. B. Cetegen and S. Basu, Review of Modeling of Liquid Precursor Droplets and Particles Injected into Plasmas and High Velocity Oxy-Fuel (HVOF) Flame Jets for Thermal Spray Applications, *J. Therm. Spray Technol.*, 2009, **18**, p 769-793
16. J. Fazilleau, C. Delbos, V. Rat, J. Coudert, P. Fauchais, and B. Pateyron, Phenomena Involved in Suspension Plasma Spraying, Part 1: Suspension Injection and Behavior, *Plasma Chem. Plasma Process.*, 2006, **26**, p 371-391
17. Y. Shan, T. Coyle, and J. Mostaghimi, Numerical Simulation of Droplet Breakup and Collision in the Solution Precursor Plasma Spraying, *J. Therm. Spray Technol.*, 2007, **16**, p 698-704
18. C. Marchand, A. Vardelle, G. Mariaux, and P. Lefort, Modeling of the Plasma Spray Process with Liquid Feedstock Injection, *Surf. Coat. Technol.*, 2008, **202**, p 4458-4464
19. S. Prakash and W. Sirignano, Theory of Convective Droplet Vaporization with Unsteady Heat Transfer in the Circulating Liquid Phase, *Int. J. Heat Mass Transf.*, 1980, **23**, p 253-268
20. B. Abramzon and W. Sirignano, Droplet Vaporization Model for Spray Combustion Calculations, *Int. J. Heat Mass Transf.*, 1989, **32**, p 1605-1618
21. G.M. Faeth, Current Status of Droplet and Liquid Combustion, *Prog. Energy Combust. Sci.*, 1977, **3**, p 191-224
22. A. Tong and W. Sirignano, Multicomponent Droplet Evaporation in a High Temperature Gas, *Combust. Flame*, 1986, **66**, p 221-235
23. M. Boulos, P. Fauchais, and E. Pfender, *Thermal Plasmas Fundamentals and Applications*, Plenum Press, New York and London, 1994
24. I. Castillo and R. Munz, Transient Modeling of Heat, Mass and Momentum Transfer of an Evaporating Cerium Nitrate Solution Droplet with a Surrounding Shell in a RF Thermal Argon-Oxygen Plasma Under Reduced Pressure, *Int. J. Heat Mass Transf.*, 2007, **50**, p 4468-4487
25. G. Jayanthi, S. Zhang, and G. Messing, Modeling of Solid Particle Formation During Solution Aerosol Thermolysis, *Aerosol Sci. Technol.*, 1993, **19**, p 478-490